

Au-Encapsulated Fe Nanorods in Oxide Matrix with Tunable Magneto-Optic Coupling Properties

Bruce Zhang, Matias Kalaswad, Bethany X. Rutherford, Shikhar Misra, Zihao He, Haohan Wang, Zhimin Qi, Ashley E. Wissel, Xiaoshan Xu, and Haiyan Wang*



Cite This: *ACS Appl. Mater. Interfaces* 2020, 12, 51827–51836



Read Online

ACCESS |



Metrics & More



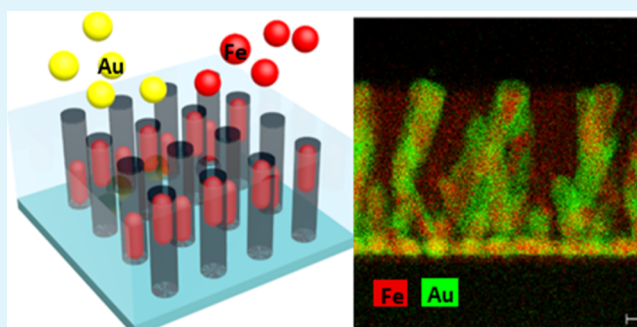
Article Recommendations



Supporting Information

ABSTRACT: Materials with magneto-optic coupling properties are highly coveted for their potential applications ranging from spintronics and optical switches to sensors. In this work, a new, three-phase Au–Fe– $\text{La}_{0.5}\text{Sr}_{0.5}\text{FeO}_3$ (LSFO) hybrid material grown in a vertically aligned nanocomposite (VAN) form has been demonstrated. This three-phase hybrid material combines the strong ferromagnetic properties of Fe and the strong plasmonic properties of Au and the dielectric nature of the LSFO matrix. More interestingly, the immiscible Au and Fe phases form Au-encapsulated Fe nanopillars, embedded in the LSFO matrix. Multifunctionalities including anisotropic optical dielectric properties, plasmonic properties, magnetic anisotropy, and room-temperature magneto-optic Kerr effect coupling are demonstrated. The single-step growth method to grow the immiscible two-metal nanostructures (i.e., Au and Fe) in the complex hybrid material form opens exciting new potential opportunities for future three-phase VAN systems with more versatile metal selections.

KEYWORDS: three-phase hybrid material, self-assembled, magneto-plasmonic, nanostructures, tunability



INTRODUCTION

Magneto-optic materials can effectively utilize light propagation to tune the magnetic spins in materials; the reverse can also occur when an applied magnetic field affects the propagation of light through the materials. These materials have recently attracted attention due to their proposed roles in a variety of different applications such as spintronics,^{1–3} waveguides,^{4,5} and optical sensors.^{6,7} As the demands for high performance, low-energy consumption, and compact devices rise, there is a crucial and pressing need to develop novel materials for effective magneto-optic coupling. To this end, various magneto-optic coupling materials have been fabricated, such as single-phased thin films (e.g., Fe and Ni),^{8–10} multilayer films (e.g., Fe/Cr/Fe and Au/Co/Au),^{11,12} and nanostructured films (e.g., split-ring nanoantennas).^{13,14} Among these candidates, nanostructures with magneto-optic coupling have received considerable interest due to their unique geometry that are used in applications such as label-free detection in biosensors^{15,16} and high-speed applications in communication devices.^{5,17} These nanostructures typically consist of either one or multiple metals fabricated into different arrays consisting of nanodisks,^{18–20} nanoparticles,^{21,22} or nanorods.^{1,23} By fabricating these metals into different nanostructures, their plasmon response is enhanced and new functionality emerges.²⁴ Typically, lithography and multistep

growth are used to fabricate these different structural arrays.^{25–27}

Vertically aligned nanocomposites (VANs) present an alternative approach for processing complex nanostructures.^{28–32} VANs can be deposited using a single-step self-assembly process that consists of two different phases arranged into a checkboard pattern or pillar-in-matrix form.^{30,33} Traditionally, a VAN consists of two oxide phases coupled together, with one oxide having strong physical properties and the other oxide having strong vertical strain that couples with the primary phase.^{28,34} Due to their unique vertical structure, VANs have a couple of main advantages compared to the conventional oxide thin films, such as highly anisotropic geometry, unique physical properties without any patterning or strict growth control,^{35,36} and multifunctionalities, for example, multiferroism.^{37–40} In addition to the significant amount of work in oxide–oxide VANs, a new class of oxide–metal VANs—such as Co– BaZrO_3 , Au– BaTiO_3 , and Ni–BZY—has recently emerged.^{41–49} Compared to the traditional oxide–

Received: August 10, 2020

Accepted: October 23, 2020

Published: November 9, 2020



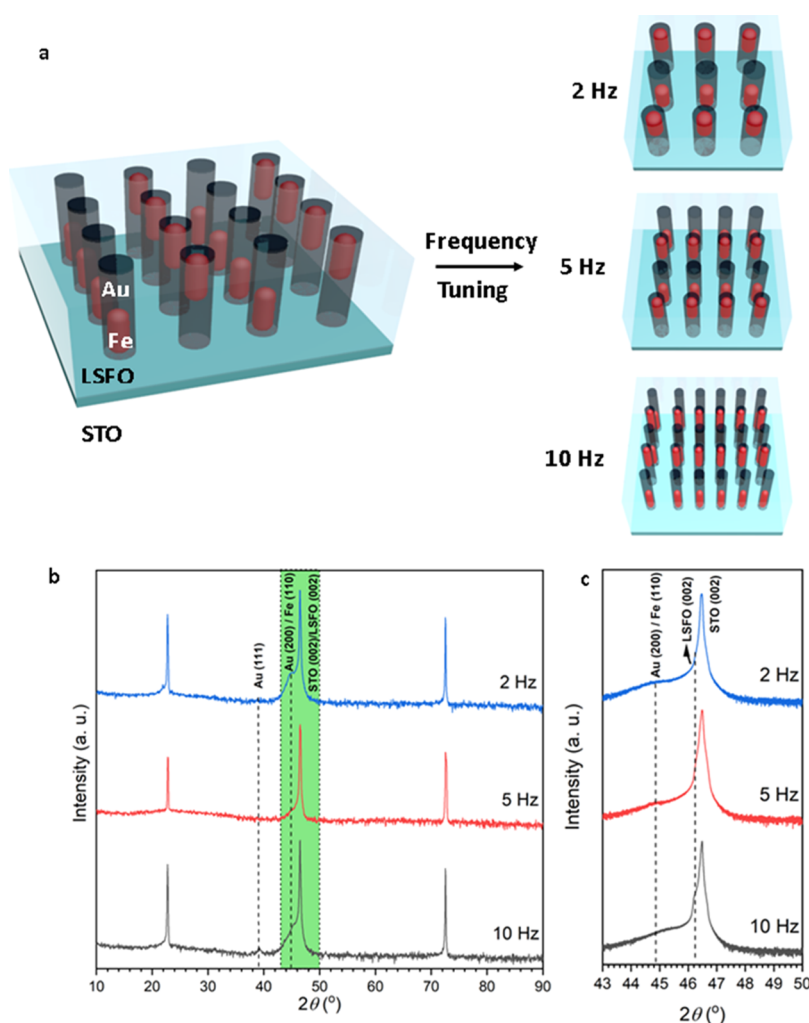


Figure 1. (a) Schematic demonstration of the growth of the Au–Fe–LSFO system. (b) Typical $\theta - 2\theta$ XRD scans of the different films deposited at different frequencies. (c) Finer $\theta - 2\theta$ XRD scans of the film between the 2θ values of 43 and 50°.

oxide systems, oxide–metal VANs include a dissimilar metallic phase, leading to stronger anisotropic properties, especially ferromagnetic and plasmonic properties. Different from the previously reported metal pillars fabricated utilizing other techniques,^{50,51} these metallic pillars are sub-100 nm in diameter and can be processed in a single-step growth process that can be integrated in devices for a large range of applications. Currently, most of the metallic pillars in VANs are single phase metal with one functionality, for example, plasmonic^{49,52,53} or ferromagnetic,^{42,44,54,55} and very limited demonstration of complex metallic nanopillars.⁴⁷

A well-coupled magnetic–plasmonic material framework is needed to fabricate stronger magneto-optical coupling. In this work, a unique composite metallic nanopillar structure coupling a plasmonic metal (e.g., Au) and a ferromagnetic metal (e.g., Fe) is proposed in a $\text{La}_{0.5}\text{Sr}_{0.5}\text{FeO}_3$ (LSFO) matrix, forming the complex three-phase metal–oxide VAN, that is, Au–Fe– $\text{La}_{0.5}\text{Sr}_{0.5}\text{FeO}_3$ (Fe–Au–LSFO), as illustrated in Figure 1. The reason that Au and Fe are selected as the metallic pillars is due to their plasmonic and ferromagnetic properties, respectively, and their immiscible nature following the Hume-Rothery rules accordingly.⁵⁶ LSFO was chosen as the oxide matrix since Fe–LSFO VANs have been successfully grown via decomposition⁵⁷ or with additional Fe inclusions,⁴¹ effectively producing strong ferromagnetic properties. Because

of the immiscible nature of Au and Fe, they will likely form two-phase pillars instead of alloyed pillars. By tuning the deposition parameters, such as deposition frequency, the morphology of the three-phase VAN can be effectively tuned. The morphology tuning alters the magnetic, magneto-optical coupling, and optical anisotropy, which is used to evaluate the property coupling and added functionalities in using the complex three-phase VAN designs.

EXPERIMENTAL SECTION

The LSFO target was prepared via the conventional sintering method with a 1:1 molar ratio of lanthanum and strontium with Fe_2O_3 into a 30 mm pellet target. The films were then grown via the pulsed laser deposition (PLD) system (KrF excimer laser) (Lambda Physik, $\lambda = 248$ nm) with a 4 mm wide pure Au strip attached to the surface of the target, onto a single crystalline SrTiO_3 (STO) (001) substrate, with the Au strip covering about 8% of the total area of the laser track on the target surface. Varying deposition frequencies of 2, 5, and 10 Hz were used to vary the nanostructure of the overall system. The frequencies were chosen with a factor of two difference to affect the growth conditions and nanostructures in a more noticeable fashion with 10 Hz being the maximum frequency selected for this study.

The nanostructure of the films was analyzed using various analytical tools. X-ray diffraction (XRD), transmission electron microscopy (TEM), scanning transmission electron microscopy (STEM), and energy-dispersive X-ray spectra (EDS) elemental mapping were

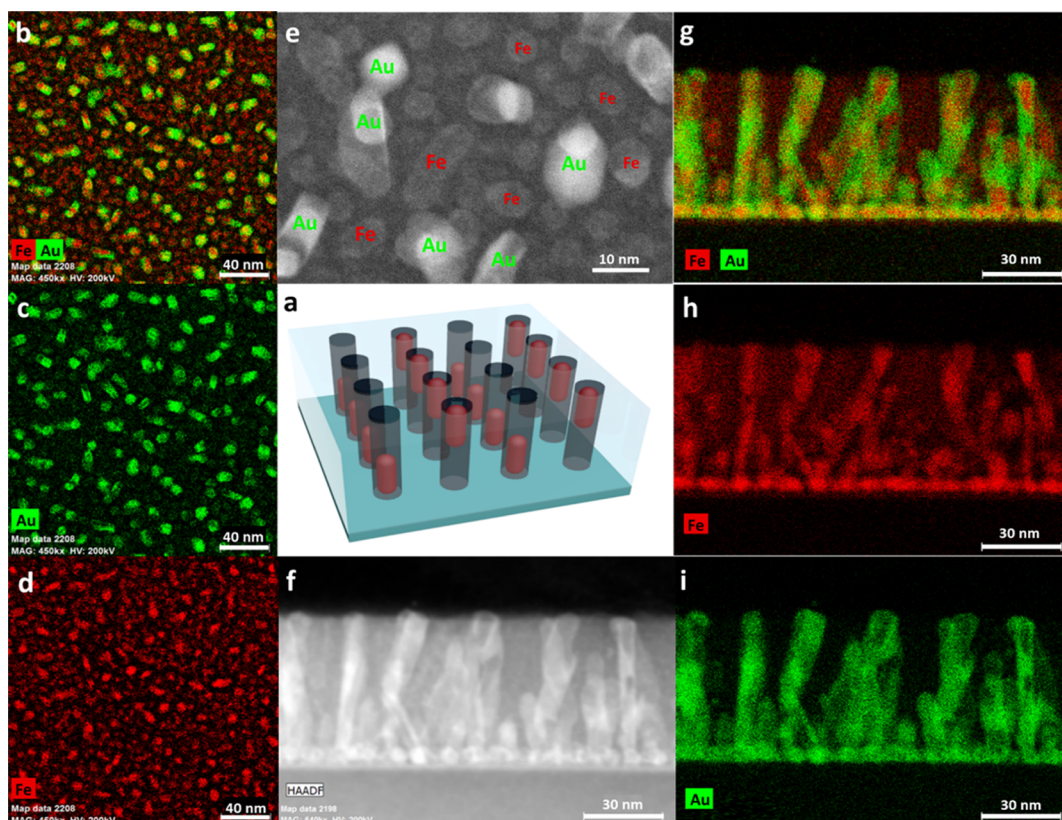


Figure 2. (a) Schematic demonstration of the Au–Fe–LSFO film grown on STO. (b–d) Plan-view EDS mappings of the 5 Hz film with (b) Fe and Au, (c) Au, and (d) Fe mappings shown. (e,f) HRSTEM image of the 5 Hz Au–Fe–LSFO film with (e) being plan-view and (f) being cross-sectional. (g–i) Cross-sectional EDS mappings of the 5 Hz film with (g) Fe and Au, (h) Fe, and (i) Au mappings shown.

performed on all samples (FEI Talos-200X). The overall film and alloy compositional analysis was performed by EDS analysis in scanning electron microscopy.

The magnetic behavior of the three-phase film was measured utilizing a magnetic property measuring system (MPMS 3, Quantum Design) for both parallel (in-plane) and perpendicular (out-of-plane) directions relative to the film surface.

The dielectric behavior of all samples grown at different frequencies was measured by using a spectroscopic ellipsometer (JA Woollam RC2) by assuming a homogenous layer and fitting an uniaxial anisotropic model using general oscillators to fit the ellipsometer parameters ψ and Δ , with this model being used in similar systems.^{45,52} The in-plane and out-of-plane permittivity was modeled using two Lorentz oscillators and a Drude–Lorentz model to enforce the Kramers–Kronig consistency, respectively.

RESULTS AND DISCUSSION

The phase composition and orientation of the Au–Fe–LSFO films deposited at different laser frequencies (2, 5, and 10 Hz) were first analyzed via typical $\theta - 2\theta$ XRD scans of the films. The XRD data in Figure 1b show the expected LSFO (002) peak with Au(111) peaks at a 2θ value of 39.1° and Au(200) and Fe(110) peaks located around 2θ values of 45.0 , 45.2 , and 45.5° for the samples deposited at 2, 5, and 10 Hz, respectively. The existence of the Fe peaks indicates that the LSFO successfully decomposed through the reaction $2\text{La}_{0.5}\text{Sr}_{0.5}\text{FeO}_3 \rightarrow \text{LaSrFeO}_4 + \text{Fe} + \text{O}_2$, as previously reported.⁵⁷ Also, the Au peaks indicate that the Au was successfully deposited as a separate phase. As the deposition frequency increases from 2 to 5 to 10 Hz, the compressive strain based on the Fe(110) peak position increases to -0.7 , -1.1 , and -1.9% , respectively, when compared to the bulk value at 44.673° (PDF # 06-0696).

This strain variation can be attributed to the varying nucleation and growth time. As the frequency decreases, the Fe and Au atoms have a longer time to diffuse, creating metallic nanostructures with more relaxed strain states. Increasing frequencies result in the Fe and Au atoms having less time to diffuse, creating more strained nanostructures.

In addition to the strain state variation, it is also important to verify whether the Au and Fe have formed the proposed two phases or an alloyed structure. Usually, Fe and Au are immiscible under equilibrium conditions following the Hume-Rothery rules. Since the PLD process introduces high kinetic energy and nonequilibrium conditions that may aid in the formation of alloyed structures, successful TEM analysis was performed to reveal the phase distribution of the three-phase VANs. TEM/STEM was instrumental in determining both the morphology of the nanostructure and phase separation of Au and Fe via plan-view TEM images of the 5 Hz Au–Fe–LSFO, as shown in Figure 2b–e. The growth of the two metal phases led to two distinct groups of structures. One type of nanostructures has a larger diameter of around 15 nm with a lower density and lighter contrast, while the other type has a smaller diameter of around 7 nm with a higher density and darker contrast. Additionally, the larger nanostructures are more faceted with a more polygonal shape, while the smaller nanostructures have a smooth, round shape. An EDS mapping was performed to specify the composition of the two nanostructures. The EDS reveals that the Au (green) are the larger nanostructures while the Fe (red) are the smaller nanostructures. From these images, it is possible to see discrete groups of both the Au and Fe, suggesting that the two metallic

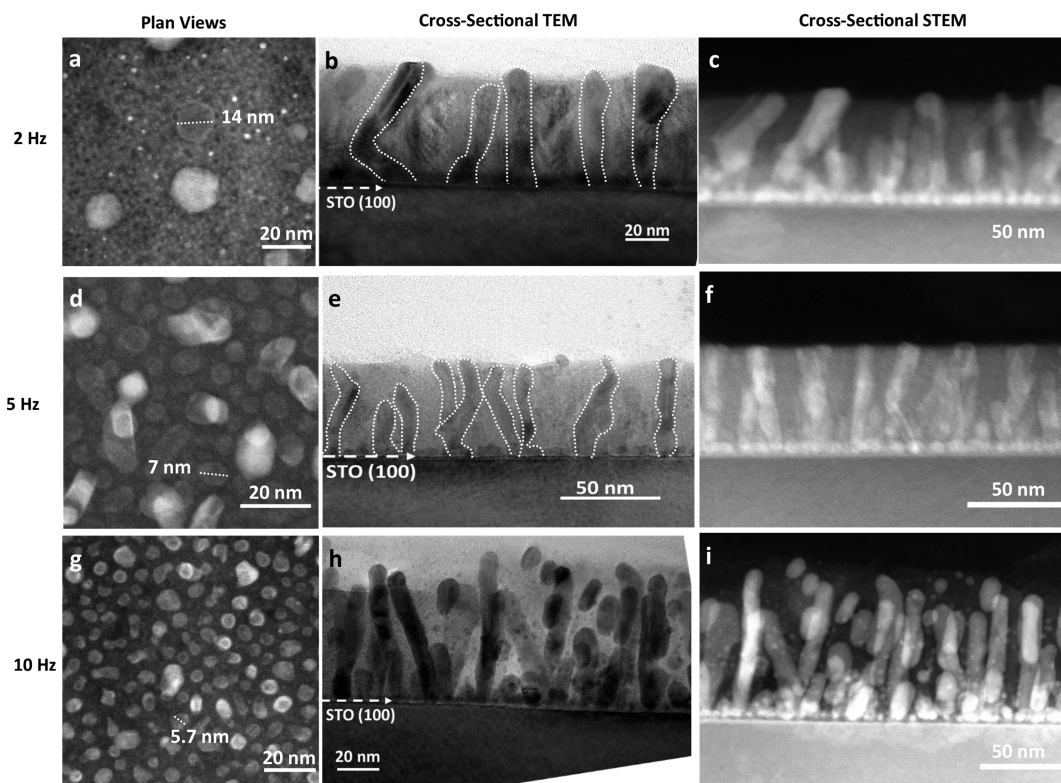


Figure 3. (a,d,g) Plan-view TEM images of the samples deposited under different frequencies to demonstrate how the Fe pillars vary. Cross-sectional (b,e,h) TEM images and (c,f,i) STEM images to better observe how the pillar structures vary with deposition frequency.

phases are formed as two phases in a unique Au-encapsulated Fe structure.

To better understand the different nanostructures, additional cross-sectional TEM images were taken of the 5 Hz Au–Fe–LSFO film. From the cross-sectional images in Figure 2f–i, it is possible to see two distinct Au–Fe morphologies in the system with the EDS mappings being displayed: (1) isotropic, metallic nanoparticles aggregated near the substrate and (2) anisotropic, column growth throughout the entirety of the film with selected columns having a slight tilt along the length of the column. The isotropic growth is most likely a result of the initial nucleation stages of the growth. In the initial stages, the Fe and Au have much higher surface energies than the LSFO, resulting in the metallic island growth. As the growth continues past the initial stage, the Fe nucleates along with Au deposition, aggregating together due to their similar surface energy compared to the oxide matrix. This causes them to find other metal adatoms, forming unique Au-encapsulated Fe nanopillars. The tilting of the nanopillars could be related to the exposing of the lower surface energy of Au(111) planes while maintaining the crystalline orientation of the nanopillars.

To investigate further how the Au and the Fe nucleate and to demonstrate the tunability of the nanostructures, the deposition frequency varied from 2, 5, and 10 Hz. TEM analysis was performed on the different samples using both the cross-section and plan-view. From the plan-view images in Figure 3, it is possible to see a change in the sizes of the Fe nanostructures with the distribution being graphed in Figure S2. As the frequency increases from 2 to 10 Hz, the Fe regions change in diameter from 12.2 to 6.2 to 8.4 nm. In a similar trend, the Au regions decrease from 14.6 to 8.1 to 8.6 nm for 2, 5, and 10 Hz, respectively. For the 10 Hz sample, there are two sizes of Au regions, one with a diameter of around 12 nm and

the other with a diameter of slightly smaller than 8 nm. The difference in the nucleation of Fe and Au comes from the fact that the Au tends to encapsulate some of the Fe pillars with some Fe pillars growing as single-phase ones. The metallic pillars are influenced by frequency, which generally causes the narrowing of the diameter as seen with higher frequency. Additionally, there is an obvious shape variation as a function of frequency. At the lower frequency (e.g., 2 Hz), the Au regions are more faceted with sharp edges and corners. As the frequency increases to 5 Hz, the shape elongates along one direction with the edges reduced, but there are still several visible edges in Au. At 10 Hz, the Au regions lose all their edges, forming a round shape similar to the Fe nanostructures. This suggests that lower frequency and longer diffusion time lead to more faceted Au nanostructures while high-frequency growth leads to more isotropic shaped nanostructures.

Cross-sectional TEM images were taken to further reveal the morphology tuning. At 2 Hz, both the Au and the Fe form pillars with a discrete shape and a large size but with selected pillars having either a 30° tilt or a vertical orientation. While for the 5 Hz growth, it is clear that the pillars are narrowed and grew in a more ordered and upright fashion. Lastly, for the 10 Hz sample, there seems to be two distinct growth morphologies, one being straight nanopillars and the other being elongated nanoparticles (nano-pill-like) within the matrix. Additionally, just as the morphology and the diameter of the nanostructures vary with frequency, the density of the metallic nanostructures also varies, i.e., the density of the pillars increases as the deposition frequency increases. The specific nanostructure variations seen between the different frequencies are likely caused by the nucleation and diffusion process. Since Au and Fe are metals which have higher surface energies when compared to the LSFO ceramic counterparts, the metallic

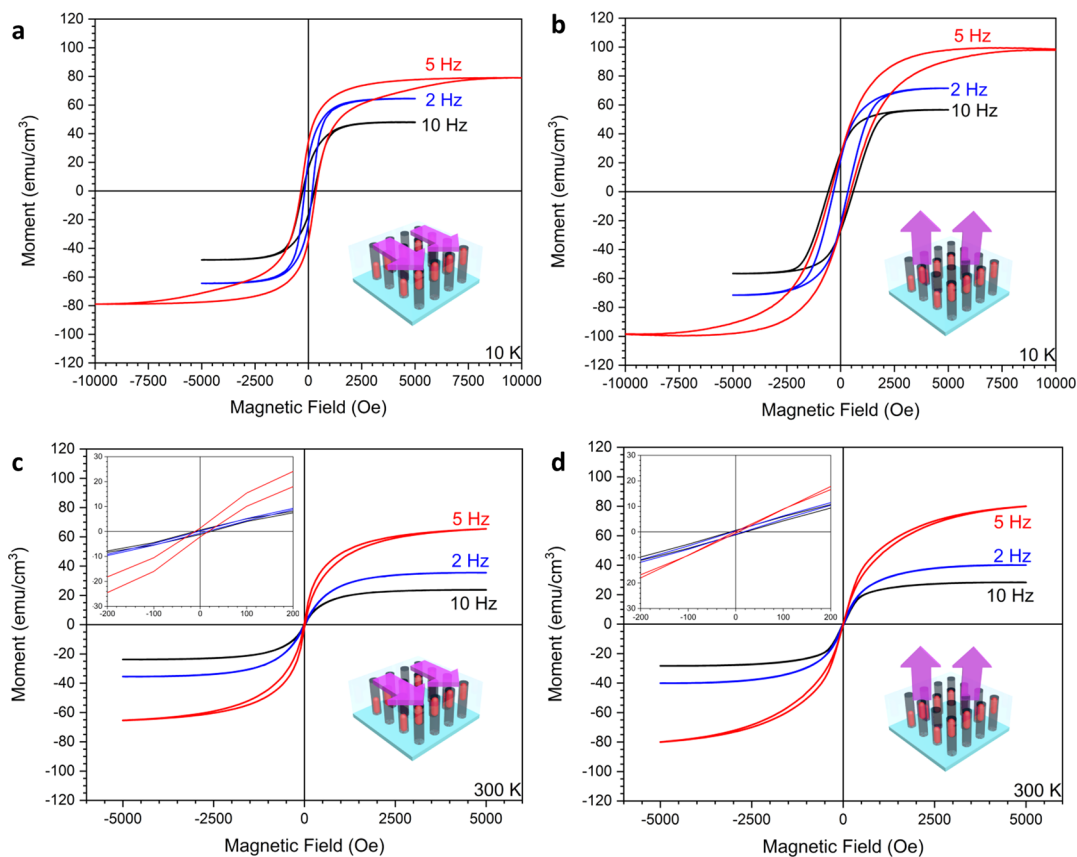


Figure 4. (a,b) Low-temperature and (c,d) room-temperature hysteresis loops of the Au–Fe–LSFO films grown at different frequencies with enlarged insets for the room-temperature loops.

adatoms will tend to accumulate as particles. In the specific cases of Au and Fe, it has been shown that Au tends to form a shell around Fe, as seen in previous works, especially at higher temperatures and growth energies.⁵⁶ In previous studies carried out on similar metal–oxide VANs, as the deposition frequency decreased, the diameter of the pillars also tends to decrease.^{44,55,58} This phenomenon is attributed to the time in between each new flux of adatoms. As frequency decreases, the adatoms will have less time to settle, causing them to form smaller, less energetically favorable, and more strained structures. As the time in between the laser shots increases, they form larger, more relaxed structures. This is consistent with the fact that at the higher frequencies, the Fe adatoms will create smaller nanostructures with the Au nucleating around these Fe structures. Furthermore, the decreased nucleation time or scarcity of Au adatoms will cause a portion of the Fe adatoms to not have sufficient time to coalesce with the existing Fe nanostructures within the Au cores. The limited time results in separated Fe nanostructure development, leading to the formation of the nano-pill-like structures seen in the 10 Hz samples. For the 2 Hz and the 5 Hz samples, the decreased frequencies lead to increased nucleation time, resulting in larger pillars in the 5 Hz and the largest Fe pillars seen in the 2 Hz sample. Au also facilitated the growth of the pillars as evidenced from a comparison between pure Fe–LSFO and Au–Fe–LSFO films grown at similar growth conditions, as shown in Figure S3. From Figure S3, the Fe regions grown in the two-phase Fe–LSFO VANs tend to grow in the nano-pill structures, yet in the three-phase Au–Fe–LSFO VAN, nanopillars occur. This can be explained by the

Au adatoms growing around the Fe regions. As the Au regions enclose the Fe regions, it makes it easier for other Au and Fe adatoms to grow on the more energetically favorable metal surfaces, resulting in the pillar growth. Additionally, the growth interactions between the substrate and the metallic nanostructures change with increasing frequency. In all different samples, there are the metallic pillars and smaller metallic uniform nanoparticles along the interface. These nanoparticles decrease in number as the frequency increases from 2 to 5 to 10 Hz. At 10 Hz, there are less nanoparticles but more discontinuous pillars when compared to both the 5 and 2 Hz samples. These nanoparticles may help relax the strain between the substrate and the film. As the adatoms have more time to diffuse, they aggregate into these small structures which result in the overall interfacial strain to decrease. In the case of the 10 Hz, the adatoms do not have time to aggregate into the nanoparticles, resulting in a higher strain as seen in the XRD. Last, frequency also varies with the atomic percentage of Au and Fe in the material. Since Au is deposited via a strip on the LSFO target, and Fe grows via decomposition, the frequency of the pulses will have a noticeable effect, as seen in Table S1. The table shows that the atomic percentage of Fe increases at 5 Hz, with a corresponding decrease in Au percentage. This may result from the 5 Hz growth promoting the growth and decomposition of Fe, resulting in the large, ordered Au–Fe growth when compared to other frequencies.

Next, to determine how the ferromagnetic behavior varies with the different nanostructures, measurements were taken from the different samples, as shown in Figure 4. At 10 K, the 2, 5, and 10 Hz have an in-plane saturation of 64, 80, and 48

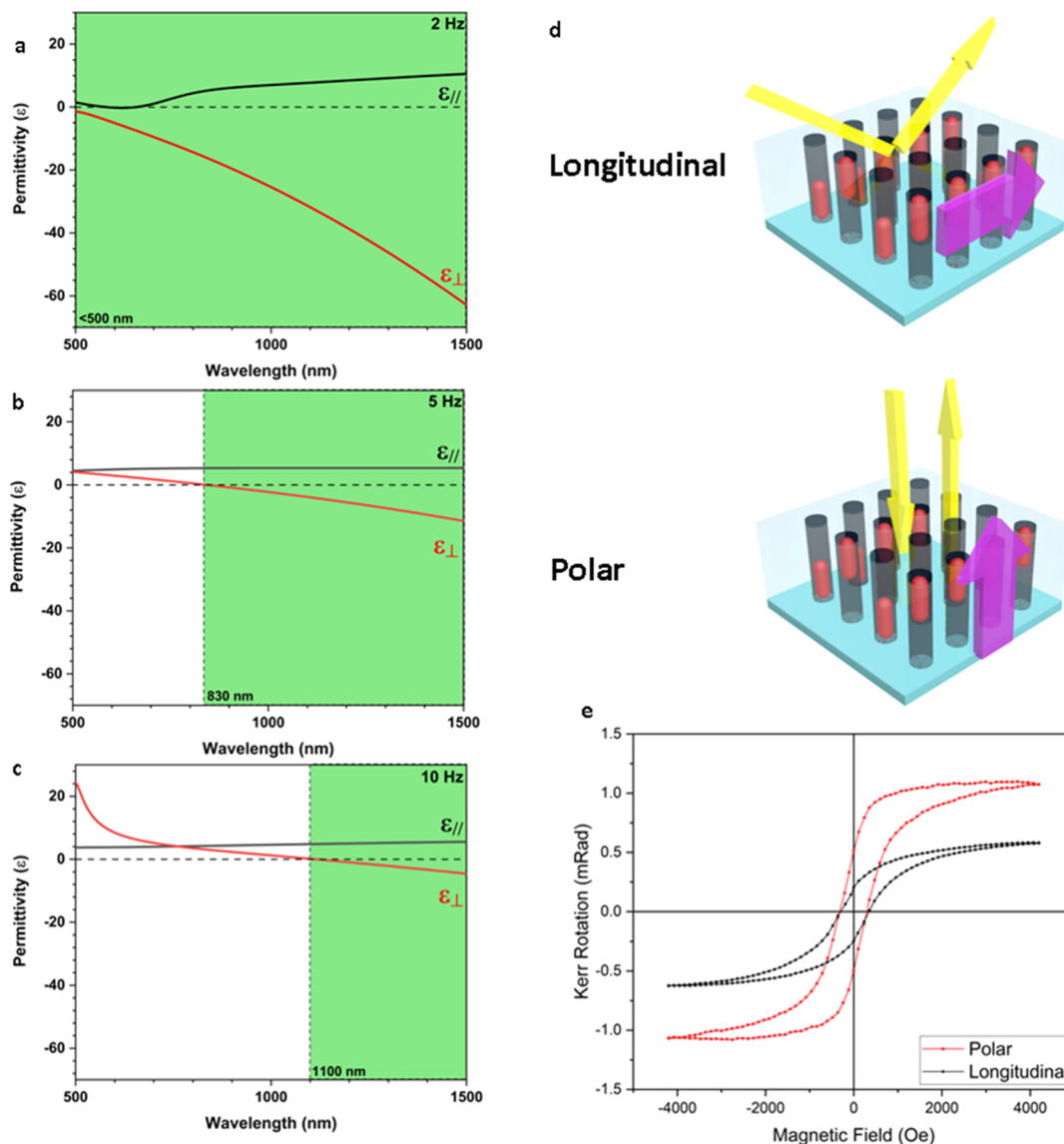


Figure 5. (a–c) Dielectric permittivity of the 2, 5, and 10 Hz sample modeled using data from the ellipsometer with green highlighting the hyperbolic region. (d) Schematic demonstration of the polar and longitudinal directions of the magneto-optic Kerr effect (MOKE) measurements where yellow is the light and purple is the applied magnetic field direction. (e) MOKE readings for the polar and longitudinal directions for the 5 Hz measurement.

emu/cm³ and out-of-plane saturation of 72, 98, and 57 emu/cm³, respectively, with an in-plane coercivity of 180, 350, and 270 Oe and out-of-plane coercivity of 330, 460, and 576 Oe, respectively. At room temperature, the 2, 5, and 10 Hz have an in-plane saturation of 35, 65, and 24 emu/cm³ and out-of-plane saturation of 40, 80, and 28 emu/cm³, respectively, with an in-plane coercivity of 10, 15, and 18 Oe and out-of-plane coercivity of 12, 5, and 15 Oe, respectively. Even though, there are similar amounts of the ferromagnetic Fe in the out-of-plane and in-plane directions, the magnetic saturations are not equal. This disparity arises from the geometry of the nanostructures. The nanostructures tend to be elongated in the out-of-plane direction, resulting in the larger out-of-plane saturation. The 5 Hz sample has the largest coercivity and magnetic saturation at low temperature due to predominately two factors. One of these factors, as seen in Table S1, is that there is a higher atomic percentage of Fe in the system, resulting in a stronger magnetic material. The second factor is the overall shape of the

Fe regions. For the 5 Hz, the Fe regions within the Au structures tend to have larger continuous structures when looking from the cross-sectional view. The smaller Au–Fe regions within the 10 Hz sample cause this frequency to have the lowest magnetization. These smaller regions will cause the magnetic direction to be easily turned, resulting in the 10 Hz film to have the weakest ferromagnetic properties. Additionally, from the room-temperature properties, it is possible to see the film demonstrates superparamagnetic properties at room temperature. This superparamagnetic behavior arises from the diameter of the pillars that tend to be sub-10 nm, the limit for Fe to exhibit superparamagnetic behavior, as reported in previous studies.⁵⁹ The 2, 5 and 10 Hz samples have superparamagnetic behavior at room temperature. As previous studies have shown, as the diameters of and sizes of the Fe regions increase, the saturation and coercivity tend to increase.⁶⁰ This phenomenon can be seen with the Au–Fe nanostructures. In the 2 Hz sample, the Au tends to dominate

the metallic regions, with Fe dispersed periodically within, causing the 5 Hz regions to have a larger Fe diameter. For the 10 Hz sample, the dispersed smaller Fe regions negatively influences the saturation. This observation results in the 5 Hz sample having the largest saturation and coercivity and the 10 Hz sample having the smallest.

To evaluate the overall optical properties, the reflectivity data and optical transmittance data were collected and analyzed. The data in Figure 5a–c show a clear anisotropy based on the out-of-plane and in-plane dielectric permittivity with the out-of-plane dielectric permittivity for all samples being negative at certain wavelengths, indicating a hyperbolic response. Interestingly, the hyperbolic transition point shifts from slightly below 500 nm at 2 Hz, to 830 nm at 5 Hz, and 1100 nm at 10 Hz, with the out-of-plane dielectric permittivity decreasing with the increasing deposition frequency. This can be explained by the variation of nanostructures for each film. For the 2 Hz sample, the metallic pillars are the most continuous and the largest, and as the frequency increases, the continuity and the size of the pillars decrease, resulting in the trends seen in the out-of-plane dielectric permittivity. For the in-plane dielectric constant, the positive values are due to the metal regions being embedded within a ceramic matrix, causing a positive permittivity as seen in conventional ceramics. Interestingly, in Figure S4a, in the in-plane 2 Hz sample, it is possible to see a plasmonic absorption response around the 610 nm wavelength, where there is a local minimum in the transmission curve. Since the 2 Hz has more ordered pillars, Au has grown in a more ordered structure, resulting in an enhanced plasmonic response. This indicates that by tuning the growth parameters, it would be possible to strengthen the plasmonic response, the ferromagnetic response, and the hyperbolic transition point, which will be useful for various applications and devices.

To evaluate the magneto-optic coupling of the Au and the Fe nanostructures, MOKE data was taken at room temperature for the 5 Hz sample. From the data, it is possible to see how the induced magnetic responses varies as the light imposes on the sample in the polar and longitudinal directions (Figure 5d). Compared to the data shown in Figure 4, the MOKE data in Figure 5e show a large degree of anisotropy that exists between the in-plane (longitudinal) and out-of-plane (transverse) directions. While the anisotropy of the MOKE is larger than the MPMS, a portion of this anisotropy may arise from the difference in the out-of-plane and in-plane dielectric constants that come from the highly anisotropic structure. While this causes the large degree of anisotropy, it has been well documented in the magneto-optic coupling that exists between the plasmonic Au and ferromagnetic Fe.⁶¹ In these structures, the interfaces between Au and Fe and the optical excitation that occurs at these interfaces causes the coupling and Kerr rotation, as seen in the MOKE graph. In these nanostructures that are more columnar in nature, as opposed to the traditional nanoparticles, has the potential to cause an increase in the coupling effect due to the greater degree of shared interfacial strain and effects. As opposed to the spherical shape of the Fe regions, the Au-encapsulated Fe nanostructures had a pillar geometry, resulting in the anisotropy seen in the MOKE data. This indicates that the Au in conjunction with the Fe played a role in the magneto-optic behavior, indicating that magneto-optical coupling between Au and Fe did occur.

This magneto-optical coupling arises from the unique Au-encapsulated Fe nanostructure in this film. For this result to be

achieved, it was crucial for minimizing Fe–Au intermixing to avoid detrimental effect on both the optical and magnetic properties. To this end, Fe and Au are ideal candidates due to their immiscibility and strong physical properties. This immiscibility minimizes the Fe and Au intermixing during the nucleation process, and instead results in the forming of the Au shell around the Fe which causes the effective magneto-optical coupling. Additionally, by adding Au to the existing Fe–LSFO system, the Au-encapsulated Fe nanostructures tend to grow into the pillar form. These pillars result in highly anisotropic optical properties with hyperbolic optical properties and a high degree of magneto-optical coupling. Further studies could consider other systems that Au can be added to: Fe–BaTiO₃,⁵⁴ Co–BaZrO₃,⁵⁵ and Ni–BaZr_{0.8}Y_{0.2}O₃.⁴⁴ Additionally, the added metal can be varied to other plasmonic metals such as Ag and Cu. This complex three-phase oxide-metal VAN utilizes immiscible metals to create a unique design for engineering complex functionalities and coupled functionalities for various optical and electronic device applications, especially pertaining to the field of spintronics, where recent work has shown the potential of magneto-optic enhancements to spintronic devices.⁶²

CONCLUSIONS

This study demonstrates the successful growth of a complex three-phase nanocomposite Au–Fe–LSFO thin film and its potential in achieving tunable physical properties, most notably, ferromagnetic and magneto-optic properties. This novel three-phase nanocomposite material combines the strong ferromagnetic properties of Fe with the strong plasmonic response of Au, creating a unique system exhibiting strong magneto-optical properties. While Fe and Au have been previously combined, this work demonstrates a new possible single-step growth method to grow nanopillars rather than the traditional nanoparticles. Additionally, via tuning the deposition frequency, it is possible to tune the nanostructures of the film, and subsequently the magnetic and optical properties for use in different applications. This study demonstrates a method to include a third phase, another metal, in the oxide–metal VAN design to provide additional functionality beyond the conventional two-phase VAN systems offer. The approach opens a new and exciting avenue for effective magneto-optical coupling toward future optical switches, sensors, and biological and spintronic devices.

ASSOCIATED CONTENT

Supporting Information

The Supporting Information is available free of charge at <https://pubs.acs.org/doi/10.1021/acsami.0c14424>.

Additional STEM and EDS images of the 2 and 10 Hz; histogram of the distribution of Fe and Au regions; STEM images of Fe–LSFO without Au; ψ , Δ , and transmission data from the ellipsometer measurements; and percentages of the metals (PDF)

AUTHOR INFORMATION

Corresponding Author

Haiyan Wang – School of Electrical and Computer Engineering and School of Materials Engineering, Purdue University, West Lafayette, Indiana 47907, United States; orcid.org/0000-0002-7397-1209; Email: hwang00@purdue.edu

Authors

Bruce Zhang – School of Electrical and Computer Engineering, Purdue University, West Lafayette, Indiana 47907, United States

Matias Kalaswad – School of Electrical and Computer Engineering, Purdue University, West Lafayette, Indiana 47907, United States

Bethany X. Rutherford – School of Materials Engineering, Purdue University, West Lafayette, Indiana 47907, United States; orcid.org/0000-0003-4149-9891

Shikhar Misra – School of Materials Engineering, Purdue University, West Lafayette, Indiana 47907, United States

Zihao He – School of Electrical and Computer Engineering, Purdue University, West Lafayette, Indiana 47907, United States

Haohan Wang – Department of Physics and Astronomy, University of Nebraska-Lincoln, Lincoln, Nebraska 68588, United States

Zhimin Qi – School of Materials Engineering, Purdue University, West Lafayette, Indiana 47907, United States

Ashley E. Wissel – School of Materials Engineering, Purdue University, West Lafayette, Indiana 47907, United States

Xiaoshan Xu – Department of Physics and Astronomy, University of Nebraska-Lincoln, Lincoln, Nebraska 68588, United States; orcid.org/0000-0002-4363-392X

Complete contact information is available at:

<https://pubs.acs.org/10.1021/acsami.0c14424>

Notes

The authors declare no competing financial interest.

ACKNOWLEDGMENTS

This work was supported by the U.S. Department of Energy, Office of Science, Basic Energy Sciences under Award DE-SC0020077. The high-resolution TEM/STEM characterization at Purdue University was supported by the U.S. National Science Foundation (DMR-1565822 and DMR-2016453). This work was partially supported by the National Science Foundation for the MOKE measurement at the University of Nebraska-Lincoln (DMR-1454618).

REFERENCES

- (1) Malaidurai, M.; Santosh Kumar, B.; Thangavel, R. Spin Polarized Carrier Injection Driven Magneto-Optical Kerr Effect in Cr-Doped ZnO Nanorods. *Phys. Lett. A* **2019**, *383*, 2988–2992.
- (2) Kumar Gudelli, V.; Guo, G.-Y. Magnetism and Magneto-Optical Effects in Bulk and Few-Layer CrI₃: A Theoretical GGA + U Study. *New J. Phys.* **2019**, *21* (). DOI: [10.1088/1367-2630/ab1ae9](https://doi.org/10.1088/1367-2630/ab1ae9).
- (3) Higo, T.; Man, H.; Gopman, D. B.; Wu, L.; Koretsune, T.; van 't Erve, O. M. J.; Kabanov, Y. P.; Rees, D.; Li, Y.; Suzuki, M.-T.; Patankar, S.; Ikhlas, M.; Chien, C. L.; Arita, R.; Shull, R. D.; Orenstein, J.; Nakatsuji, S. Large Magneto-Optical Kerr Effect and Imaging of Magnetic Octupole Domains in an Antiferromagnetic Metal. *Nat. Photonics* **2018**, *12*, 73–78.
- (4) Kreilkamp, L. E.; Belotelov, V. I.; Chin, J. Y.; Neutzner, S.; Dregely, D.; Wehler, T.; Akimov, I. A.; Bayer, M.; Stritzker, B.; Giessen, H. Waveguide-Plasmon Polaritons Enhance Transverse Magneto-Optical Kerr Effect. *Phys. Rev. X* **2014**, *3*, 1–7.
- (5) Dötsch, H.; Bahlmann, N.; Zhurumskyy, O.; Hammer, M.; Wilkens, L.; Gerhardt, R.; Hertel, P.; Popkov, A. F. Applications of Magneto-Optical Waveguides in Integrated Optics: Review. *J. Opt. Soc. Am. B* **2005**, *22*, 240.
- (6) Shiyu, Y.; Lousteau, J.; Olivero, M.; Merlo, M.; Boetti, N.; Abrate, S.; Chen, Q.; Chen, Q.; Milanese, D. Analysis of Faraday

Effect in Multimode Tellurite Glass Optical Fiber for Magneto-Optical Sensing and Monitoring Applications. *Appl. Opt.* **2012**, *51*, 4542–4546.

(7) Manera, M. G.; Colombelli, A.; Rella, R.; Caricato, A.; Cozzoli, P. D.; Martino, M.; Vasanelli, L. TiO₂ Brookite Nanostructured Thin Layer on Magneto-Optical Surface Plasmon Resonance Transducer for Gas Sensing Applications. *J. Appl. Phys.* **2012**, *112*, 053524.

(8) Buchmeier, M.; Schreiber, R.; Bürgler, D. E.; Schneider, C. M. Thickness Dependence of Linear and Quadratic Magneto-Optical Kerr Effects in Ultrathin Fe(001) Films. *Phys. Rev. B: Condens. Matter Mater. Phys.* **2009**, *79*, 1–7.

(9) Mok, K.; Scarlet, C.; Kovács, G. J.; Li, L.; Zviagin, V.; McCord, J.; Helm, M.; Schmidt, H. Thickness Independent Magneto-Optical Coupling Constant of Nickel Films in the Visible Spectral Range. *J. Appl. Phys.* **2011**, *110*, 123110.

(10) Mok, K.; Kovács, G. J.; McCord, J.; Li, L.; Helm, M.; Schmidt, H. Magneto-Optical Coupling in Ferromagnetic Thin Films Investigated by Vector-Magneto-Optical Generalized Ellipsometry. *Phys. Rev. B: Condens. Matter Mater. Phys.* **2011**, *84*, 1–6.

(11) Schäfer, R. Magneto-Optical Domain Studies in Coupled Magnetic Multilayers. *J. Magn. Magn. Mater.* **1995**, *148*, 226–231.

(12) Hermann, C.; Kosobukin, V.; Lampel, G.; Peretti, J.; Safarov, V.; Bertrand, P. Surface-Enhanced Magneto-Optics in Metallic Multilayer Films. *Phys. Rev. B: Condens. Matter Mater. Phys.* **2001**, *64*, 1–11.

(13) Leslie-Pelecky, D. L.; Rieke, R. D. Magnetic Properties of Nanostructured Materials. *Chem. Mater.* **1996**, *8*, 1770–1783.

(14) Feng, H. Y.; Luo, F.; Arenal, R.; Henrard, L.; García, F.; Armelles, G.; Cebollada, A. Active Magnetoplasmonic Split-Ring/Ring Nanoantennas. *Nanoscale* **2017**, *9*, 37–44.

(15) Maksymov, I. S. Magneto-Plasmonic Nanoantennas: Basics and Applications. *Phys. Rev.* **2016**, *1*, 36–51.

(16) Larsson, E. M.; Alegret, J.; Käll, M.; Sutherland, D. S. Sensing Characteristics of NIR Localized Surface Plasmon Resonances in Gold Nanorings for Application as Ultrasensitive Biosensors. *Nano Lett.* **2007**, *7*, 1256–1263.

(17) Feng, H. Y.; Luo, F.; Kekesi, R.; Granados, D.; Meneses-Rodríguez, D.; García, J. M.; García-Martín, A.; Armelles, G.; Cebollada, A. Magnetoplasmonic Nanorings as Novel Architectures with Tunable Magneto-Optical Activity in Wide Wavelength Ranges. *Adv. Opt. Mater.* **2014**, *2*, 612–617.

(18) Bantí, J. C.; Meneses-Rodríguez, D.; García, F.; González, M. U.; García-Martín, A.; Cebollada, A.; Armelles, G. High Magneto-Optical Activity and Low Optical Losses in Metal-Dielectric Au/Co/Au-SiO₂ Magnetoplasmonic Nanodisks. *Adv. Mater.* **2012**, *24* (). DOI: [10.1002/adma.201103634](https://doi.org/10.1002/adma.201103634).

(19) Maccaferri, N.; Kataja, M.; Bonanni, V.; Bonetti, S.; Pirzadeh, Z.; Dmitriev, A.; Van Dijken, S.; Åkerman, J.; Vavassori, P. Effects of a Non-Absorbing Substrate on the Magneto-Optical Kerr Response of Plasmonic Ferromagnetic Nanodisks. *Phys. Status Solidi A* **2014**, *211*, 1067–1075.

(20) Freire-Fernández, F.; Kataja, M.; van Dijken, S. Surface-Plasmon-Polariton-Driven Narrow-Linewidth Magneto-Optics in Ni Nanodisk Arrays. *Nanophotonics* **2019**, *9*, 113–121.

(21) Erdem, D.; Bingham, N. S.; Heiligt, F. J.; Pilet, N.; Warnicke, P.; Heyderman, L. J.; Niederberger, M. CoFe₂O₄ and CoFe₂O₄-SiO₂ Nanoparticle Thin Films with Perpendicular Magnetic Anisotropy for Magnetic and Magneto-Optical Applications. *Adv. Funct. Mater.* **2016**, *26*, 1954–1963.

(22) Varytis, P.; Pantazopoulos, P. A.; Stefanou, N. Enhanced Faraday Rotation by Crystals of Core-Shell Magnetoplasmonic Nanoparticles. *Phys. Rev. B* **2016**, *93*, 1–7.

(23) Choi, B. C.; Xu, H.; Hajisalem, G.; Gordon, R. Localized Surface Plasmon Resonance Enhanced Magneto-Optical Kerr Effect in Ni₈₀Fe₂₀ Thin Films Coated with Au Nanorods. *Appl. Phys. Lett.* **2018**, *112*, 022403.

(24) Manera, M. G.; Colombelli, A.; Taurino, A.; Martin, A. G.; Rella, R. Magneto-Optical Properties of Noble-Metal Nanostructures: Functional Nanomaterials for Bio Sensing. *Sci. Rep.* **2018**, *8*, 1–12.

- (25) Loughran, T. H. J.; Roth, J.; Keatley, P. S.; Hendry, E.; Barnes, W. L.; Hicken, R. J.; Einsle, J. F.; Amy, A.; Hendren, W.; Bowman, R. M.; Dawson, P. Design and Fabrication of Plasmonic Cavities for Magneto-Optical Sensing. *AIP Adv.* **2018**, *8*, 055207.
- (26) Galvez, F.; del Valle, J.; Gomez, A.; Osorio, M. R.; Granados, D.; Pérez de Lara, D.; García, M. A.; Vicent, J. L. Plasmonic Nanodevice with Magnetic Functionalities: Fabrication and Characterization. *Opt. Mater. Express* **2016**, *6*, 3086.
- (27) Atmatzakis, E.; Papasimakis, N.; Fedotov, V. A.; Zheludev, N. I. Giant Kerr Rotation Enhancement in Magneto-Plasmonic Metamaterials. *Optics InfoBase Conference Papers*, 2014.
- (28) Chen, A.; Bi, Z.; Jia, Q.; MacManus-Driscoll, J. L.; Wang, H. Microstructure, Vertical Strain Control and Tunable Functionalities in Self-Assembled, Vertically Aligned Nanocomposite Thin Films. *Acta Mater.* **2013**, *61*, 2783–2792.
- (29) Huang, J.; MacManus-Driscoll, J. L.; Wang, H. New Epitaxy Paradigm in Epitaxial Self-Assembled Oxide Vertically Aligned Nanocomposite Thin Films. *J. Mater. Res.* **2017**, *32*, 4054–4066.
- (30) MacManus-Driscoll, J. L.; Suwardi, A.; Wang, H. Composite Epitaxial Thin Films: A New Platform for Tuning, Probing, and Exploiting Mesoscale Oxides. *MRS Bull.* **2015**, *40*, 933–942.
- (31) Zhang, W.; Chen, A.; Bi, Z.; Jia, Q.; MacManus-Driscoll, J. L.; Wang, H. Interfacial Coupling in Heteroepitaxial Vertically Aligned Nanocomposite Thin Films: From Lateral to Vertical Control. *Curr. Opin. Solid State Mater. Sci.* **2014**, *18*, 6–18.
- (32) Fan, M.; Wang, H.; Misra, S.; Zhang, B.; Qi, Z.; Sun, X.; Huang, J.; Wang, H. Microstructure, Magnetic, and Magnetoresistance Properties of La_{0.7}Sr_{0.3}MnO₃:CuO Nanocomposite Thin Films. *ACS Appl. Mater. Interfaces* **2018**, *10*, 5779–5784.
- (33) Zhang, W.; Ramesh, R.; MacManus-Driscoll, J. L.; Wang, H. Multifunctional, Self-Assembled Oxide Nanocomposite Thin Films and Devices. *MRS Bull.* **2015**, *40*, 736–745.
- (34) Huang, J.; MacManus-Driscoll, J. L.; Wang, H. New Epitaxy Paradigm in Epitaxial Self-Assembled Oxide Vertically Aligned Nanocomposite Thin Films. *J. Mater. Res.* **2017**, *32*, 4054–4066.
- (35) Zhang, W.; Li, L.; Lu, P.; Fan, M.; Su, Q.; Khatkhatay, F.; Chen, A.; Jia, Q.; Zhang, X.; MacManus-Driscoll, J. L.; Wang, H. Perpendicular Exchange-Biased Magnetotransport at the Vertical Heterointerfaces in La_{0.7}Sr_{0.3}MnO₃:NiO Nanocomposites. *ACS Appl. Mater. Interfaces* **2015**, *7*, 21646–21651.
- (36) Fan, M.; Zhang, W.; Jian, J.; Huang, J.; Wang, H. Strong Perpendicular Exchange Bias in Epitaxial La_{0.7}Sr_{0.3}MnO₃:LaFeO₃ Nanocomposite Thin Films. *APL Mater.* **2016**, *4*, 076105.
- (37) Huang, J.; Tsai, C.-F.; Chen, L.; Jian, J.; Khatkhatay, F.; Yu, K.; Wang, H. Magnetic Properties of (CoFe₂O₄)_x(CeO₂)_{1-x} Vertically Aligned Nanocomposites and Their Pinning Properties in YBa₂Cu₃O_{7- δ} Thin Films. *J. Appl. Phys.* **2014**, *115*, 123902.
- (38) Su, Q.; Yoon, D.; Chen, A.; Khatkhatay, F.; Manthiram, A.; Wang, H. Vertically Aligned Nanocomposite Electrolytes with Superior Out-of-Plane Ionic Conductivity for Solid Oxide Fuel Cells. *J. Power Sources* **2013**, *242*, 455–463.
- (39) Chen, A.; Zhou, H.; Bi, Z.; Zhu, Y.; Luo, Z.; Bayraktaroglu, A.; Phillips, J.; Choi, E.-M.; MacManus-Driscoll, J. L.; Pennycook, S. J.; Narayan, J.; Jia, Q.; Zhang, X.; Wang, H. A New Class of Room-Temperature Multiferroic Thin Films with Bismuth-Based Supercell Structure. *Adv. Mater.* **2013**, *25*, 1028–1032.
- (40) Gao, X.; Li, L.; Jian, J.; Wang, H.; Fan, M.; Huang, J.; Wang, X.; Wang, H. Vertically Aligned Nanocomposite BaTiO₃:YMnO₃ Thin Films with Room Temperature Multiferroic Properties toward Nanoscale Memory Devices. *ACS Appl. Nano Mater.* **2018**, *1*, 2509–2514.
- (41) Zhang, B.; Fan, M.; Li, L.; Jian, J.; Huang, J.; Wang, H.; Kalaswad, M.; Wang, H. Tunable Magnetic Anisotropy of Self-Assembled Fe Nanostructures within a La_{0.5}Sr_{0.5}FeO₃ Matrix. *Appl. Phys. Lett.* **2018**, *112*, 013104.
- (42) Zhang, B.; Huang, J.; Jian, J.; Rutherford, B. X.; Li, L.; Misra, S.; Sun, X.; Wang, H. Tuning Magnetic Anisotropy in Co-BaZrO₃ Vertically Aligned Nanocomposites for Memory Device Integration. *Nanoscale Adv.* **2019**, *1*, 4450–4458.
- (43) Huang, J.; Li, L.; Lu, P.; Qi, Z.; Sun, X.; Zhang, X.; Wang, H. Self-Assembled Co-BaZrO₃ Nanocomposite Thin Films with Ultra-Fine Vertically Aligned Co Nanopillars. *Nanoscale* **2017**, *9*, 7970–7976.
- (44) Su, Q.; Zhang, W.; Lu, P.; Fang, S.; Khatkhatay, F.; Jian, J.; Li, L.; Chen, F.; Zhang, X.; Macmanus-Driscoll, J. L.; Chen, A.; Jia, Q.; Wang, H. Self-Assembled Magnetic Metallic Nanopillars in Ceramic Matrix with Anisotropic Magnetic and Electrical Transport Properties. *ACS Appl. Mater. Interfaces* **2016**, *8*, 20283–20291.
- (45) Misra, S.; Li, L.; Jian, J.; Huang, J.; Wang, X.; Zemlyanov, D.; Jang, J.-W.; Ribeiro, F. H.; Wang, H. Tailorable Au Nanoparticles Embedded in Epitaxial TiO₂ Thin Films for Tunable Optical Properties. *ACS Appl. Mater. Interfaces* **2018**, *10*, 32895–32902.
- (46) Wang, X.; Jian, J.; Diaz-Amaya, S.; Kumah, C. E.; Lu, P.; Huang, J.; Lim, D. G.; Pol, V. G.; Youngblood, J. P.; Boltasseva, A.; Stanciu, L. A.; O'Carroll, D. M.; Zhang, X.; Wang, H. Hybrid Plasmonic Au-TiN Vertically Aligned Nanocomposites: A Nanoscale Platform towards Tunable Optical Sensing. *Nanoscale Adv.* **2019**, *1*, 1045–1054.
- (47) Paldi, R. L.; Sun, X.; Wang, X.; Zhang, X.; Wang, H. Strain-Driven In-Plane Ordering in Vertically Aligned ZnO-Au Nanocomposites with Highly Correlated Metamaterial Properties. *ACS Omega* **2020**, *5*, 2234–2241.
- (48) Kalaswad, M.; Zhang, D.; Gao, X.; Contreras, L. L.; Wang, H.; Wang, X.; Wang, H. Integration of Hybrid Plasmonic Au-BaTiO₃ Metamaterial on Silicon Substrates. *ACS Appl. Mater. Interfaces* **2019**, *11*, 45199–45206.
- (49) Zhang, D.; Misra, S.; Li, L.; Wang, X.; Jian, J.; Lu, P.; Gao, X.; Sun, X.; Qi, Z.; Kalaswad, M.; Zhang, X.; Wang, H. Tunable Optical Properties in Self-Assembled Oxide-Metal Hybrid Thin Films via Au-Phase Geometry Control: From Nanopillars to Nanodisks. *Adv. Opt. Mater.* **2020**, *8*, 1901359.
- (50) Kim, S.; Park, S.; Kwon, S. Y.; Nichols, W. T.; Park, W. I. Nanoscale Metal Pillar Arrays on Elastomeric Substrates for Surface-Enhanced Raman Spectroscopy Platform. *Curr. Appl. Phys.* **2015**, *15*, 711–716.
- (51) Robbie, K.; Shafai, C.; Brett, M. J. Thin Films with Nanometer-Scale Pillar Microstructure. *J. Mater. Res.* **1999**, *14*, 3158–3163.
- (52) Misra, S.; Li, L.; Zhang, D.; Jian, J.; Qi, Z.; Fan, M.; Chen, H.-T.; Zhang, X.; Wang, H. Self-Assembled Ordered Three-Phase Au-BaTiO₃-ZnO Vertically Aligned Nanocomposites Achieved by a Templating Method. *Adv. Mater.* **2019**, *31*, 1806529.
- (53) Li, L.; Sun, L.; Gomez-Diaz, J. S.; Hogan, N. L.; Lu, P.; Khatkhatay, F.; Zhang, W.; Jian, J.; Huang, J.; Su, Q.; Fan, M.; Jacob, C.; Li, J.; Zhang, X.; Jia, Q.; Sheldon, M.; Alù, A.; Li, X.; Wang, H. Self-Assembled Epitaxial Au-Oxide Vertically Aligned Nanocomposites for Nanoscale Metamaterials. *Nano Lett.* **2016**, *16*, 3936–3943.
- (54) Zhang, B.; Huang, J.; Rutherford, B. X.; Lu, P.; Misra, S.; Kalaswad, M.; He, Z.; Gao, X.; Sun, X.; Li, L.; Wang, H. Tunable, Room-Temperature Multiferroic Fe-BaTiO₃ Vertically Aligned Nanocomposites with Perpendicular Magnetic Anisotropy. *Mater. Today Nano* **2020**, *11*, 100083.
- (55) Huang, J.; Li, L.; Lu, P.; Qi, Z.; Sun, X.; Zhang, X.; Wang, H. Self-Assembled Co-BaZrO₃ Nanocomposite Thin Films with Ultra-Fine Vertically Aligned Co Nanopillars. *Nanoscale* **2017**, *9*, 7970–7976.
- (56) Tymoczko, A.; Kamp, M.; Prymak, O.; Rehbock, C.; Jakobi, J.; Schürmann, U.; Kienle, L.; Barcikowski, S. How the Crystal Structure and Phase Segregation of Au-Fe Alloy Nanoparticles Are Ruled by the Molar Fraction and Size. *Nanoscale* **2018**, *10*, 16434–16437.
- (57) Mohaddes-Ardabili, L.; Zheng, H.; Ogale, S. B.; Hannoyer, B.; Tian, W.; Wang, J.; Lofland, S. E.; Shinde, S. R.; Zhao, T.; Jia, Y.; Salamanca-Riba, L.; Schlom, D. G.; Wuttig, M.; Ramesh, R. Self-Assembled Single-Crystal Ferromagnetic Iron Nanowires Formed by Decomposition. *Nat. Mater.* **2004**, *3*, 533–538.
- (58) Huang, J.; Qi, Z.; Li, L.; Wang, H.; Xue, S.; Zhang, B.; Zhang, X.; Wang, H. Self-Assembled Vertically Aligned Ni Nanopillars in CeO₂ with Anisotropic Magnetic and Transport Properties for Energy Applications. *Nanoscale* **2018**, *10*, 17182–17188.

(59) Huber, D. L. Synthesis, Properties, and Applications of Iron Nanoparticles. *Small* **2005**, *1*, 482–501.

(60) Jacobs, I. S.; Bean, C. P. Fine Particles, Thin Films and Exchange Anisotropy (Effects of Finite Dimensions and Interfaces on the Basic Properties of Ferromagnets). *Spin Arrangements and Crystal Structure, Domains, and Micromagnetics*; Elsevier, 1963; pp 271–350.

(61) Bansmann, J.; Baker, S.; Binns, C.; Blackman, J.; Bucher, J.; Dorantesdávila, J.; Dupuis, V.; Favre, L.; Kechrakos, D.; Kleibert, A. Magnetic and Structural Properties of Isolated and Assembled Clusters. *Surf. Sci. Rep.* **2005**, *56*, 189–275.

(62) Dutta, A.; Kildishev, A. V.; Shalaev, V. M.; Boltasseva, A.; Marinero, E. E. Surface-Plasmon Opto-Magnetic Field Enhancement for All-Optical Magnetization Switching. *Opt. Mater. Express* **2017**, *7*, 4316.